Observation of topological valley modes in an elastic hexagonal lattice

Javier Vila* and Raj Kumar Pal
School of Aerospace Engineering, Georgia Institute of Technology, Atlanta, Georgia 30332, USA

Massimo Ruzzene
School of Aerospace Engineering and School of Mechanical Engineering, Georgia Institute of Technology, Atlanta, Georgia 30332, USA

(Received 14 May 2017; revised manuscript received 29 August 2017; published 17 October 2017)

We report on the experimental observation of topologically protected edge waves in a two-dimensional elastic hexagonal lattice. The lattice is designed to feature K-point Dirac cones that are well separated from the other numerous elastic wave modes characterizing this continuous structure. We exploit the arrangement of localized masses at the nodes to break mirror symmetry at the unit-cell level, which opens a frequency band gap. This produces a nontrivial band structure that supports topologically protected edge states along the interface between two realizations of the lattice obtained through mirror symmetry. Detailed numerical models support the investigations of the occurrence of the edge states, while their existence is verified through full-field experimental measurements. The test results show the confinement of the topologically protected edge states along predefined interfaces and illustrate the lack of significant backscattering at sharp corners. Experiments conducted on a trivial waveguide in an otherwise uniformly periodic lattice reveal the inability of a perturbation to propagate and its sensitivity to backscattering, which suggests the superior waveguiding performance of the class of nontrivial interfaces investigated herein.

DOI: 10.1103/PhysRevB.96.134307

I. INTRODUCTION

Wave propagation in periodic media has been an active field of research for the past few decades. Energy transport by waves arises in multiple areas of physics as it relates to acoustic, elastic, electromagnetic, and electronic media. Unique phenomena like negative refraction, directional propagation, focusing, and cloaking have been pursued through careful engineering of the band structure, which is a unifying theme for exploration in this diverse set of physical domains. Recently, the advent of topological mechanics [1] has provided an effective framework for the pursuit of robust wave propagation which is protected against perturbations and defects. Topologically protected edge wave propagation was originally envisioned in quantum systems and has quickly evolved to other classical areas of physics, such as acoustics [2], photonics [3,4], and mechanics [5,6], as well as to coupled-wave domains such as optomechanics [7]. In all of these different domains, properties such as lossless propagation, existence of waves confined to a boundary or interface, immunity to backscattering, and localization in the presence of defects and imperfections are the result of band topology. This makes them classical analogs of topological insulators that support the propagation of topologically protected edge waves (TPEWs).

There are two broad ways to realize topologically protected wave propagation in elastic media. The first one uses active components, thereby mimicking the quantum Hall effect. Changing the parity of active devices or modulating the physical properties in time, for example, has been shown to alter the direction and nature of edge waves [8,9]. Examples include magnetic fields in biological systems [10], rotating disks [11], and acoustic circulators operating on the basis of a flow-induced bias [12]. A second way uses solely passive components and relies on establishing analogs of the quantum spin Hall effect. These media feature both forward- and backward-propagating edge modes, which can be induced by an external excitation of appropriate polarization. The concept is illustrated in several studies by way of both numerical [5,13,14] and experimental [15,16] investigations, which involve coupled pendulums [15], plates with two-scale holes [5], and resonators [13], as well as electric circuits [16]. Numerous studies have also been conducted on localized nonpropagating deformation modes at the interface of two structural lattices [6,17,18]. These modes depend on the topological properties of the bands, which in one-dimensional lattices are characterized by the Zak phase as a topological invariant [19]. In two- and three-dimensional lattices, several researchers have investigated the presence of floppy modes of motion due to nontrivial topological polarization and exploited these modes to achieve localized buckling and directional response [20–23]. In spite of the intense level of activity in this area, to the best of our knowledge, studies reporting on the experimental observation of TPEWs in continuous elastic media have so far been limited. Unique challenges in elastic systems exist due to their high modal densities, which complicate the analysis and design of the band structure and the effective achievement of nontrivial topologies. These also often lead to complex arrangements of materials and intricate connectivities that may be hard to realize in practice. A promising avenue in this regard is the use of valley degrees of freedom as originally envisioned in quantum systems like graphene bilayers [24–26]. The concept has also been adopted in classical areas such as photonics [4,27], acoustics [28–30], and phononics [2,6].

The objective of this study is to exploit valley degrees of freedom to obtain and demonstrate experimentally TPEWs in continuous elastic media. The considered configuration consists of an elastic hexagonal lattice on which concentrated masses are attached at the sublattice sites. This provides

*javier.vila@aerospace.gatech.edu

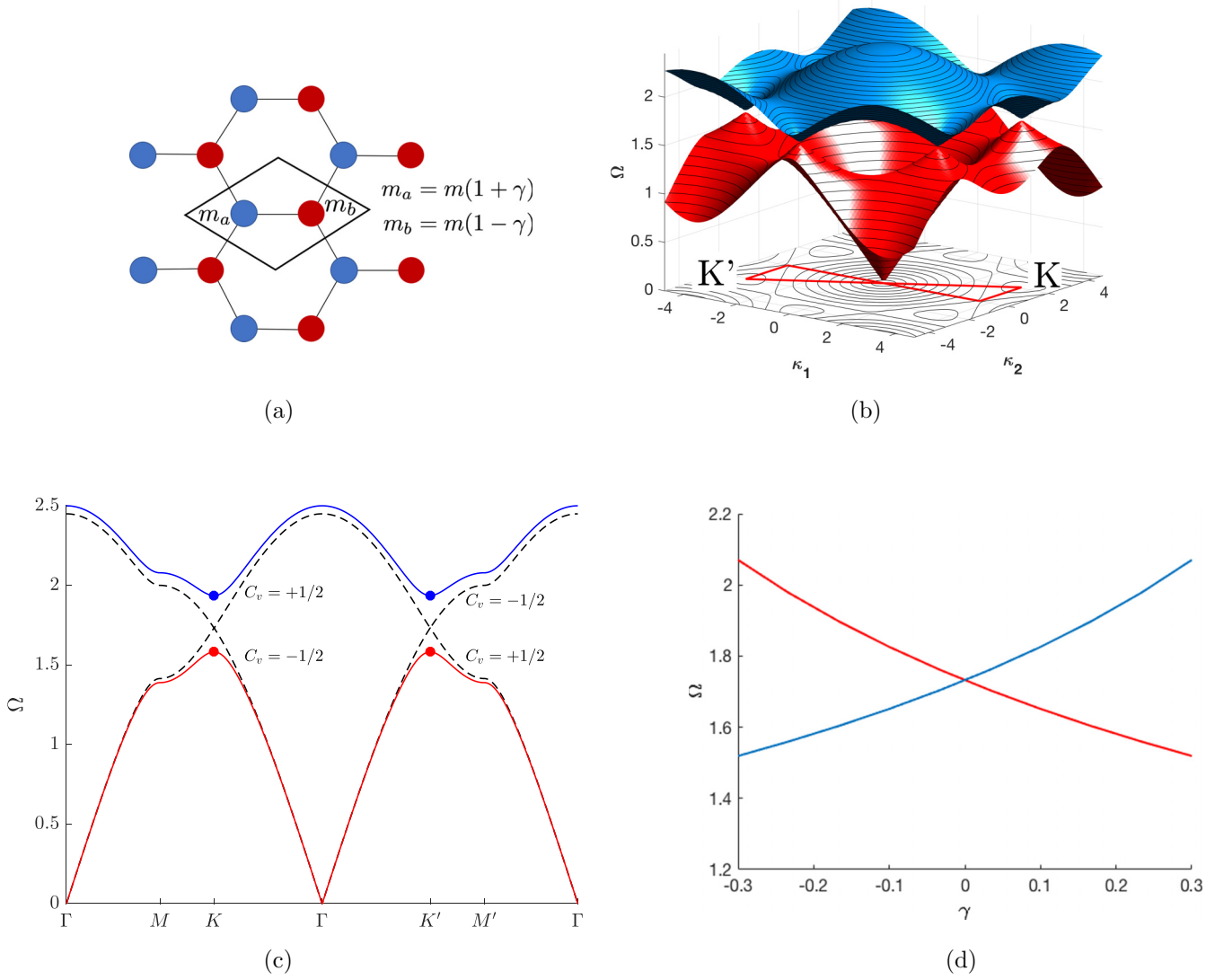

FIG. 1. (a) Hexagonal discrete lattice emulating the QVHE. (b) Dispersion surfaces and contours of the first surface for $\gamma = 0$, highlighting the presence of Dirac cones, the first irreducible Brillouin zone (solid red line), and the location of the K and K' points. (c) Band diagrams reporting the values of the valley Chern numbers at the K and K' points for $\gamma = 0$ (dashed black line) and $\gamma = +0.2$ (solid red and blue lines). (d) Inversion of the bounding frequencies of the band gap as a function of the parameter γ.

a simple assembly that is characterized by the symmetry conditions sufficient to open a topologically nontrivial band gap. The addition of masses at selected locations within a unit cell breaks the C_{3v} symmetry inherent in the hexagonal geometry while preserving the C_3 symmetry. Exploiting the arrangement of masses conveniently leads to lattices that exhibit different topological properties of the bands. When two such lattices with different topological properties are joined together, TPEWs propagate along the shared interface.

The outline of this paper is as follows: Sec. II explains the concept of valley modes, while Sec. III presents the description of the continuous hexagonal lattice, along with its dispersion analysis and the dispersion analysis of a finite strip containing an interface. Section IV describes the experimental setup, the estimation of the dispersion diagrams for the lattices, and results showing TPEWs for two different interfaces. Finally, Sec. V summarizes the main results of this study and presents potential future research directions.

II. HEXAGONAL SPRING-MASS LATTICES AND VALLEY HALL EFFECT ANALOGY

We briefly illustrate the quantum valley Hall effect (QVHE) analogy for discrete hexagonal lattices, which provide the basic configuration for the design and subsequent study of the continuous lattices investigated herein. While detailed descriptions of the concept can be found in [6], we briefly review how changes in topological properties can be achieved by considering unit cells that are inverted copies of each other, leading to band inversion in the dispersion diagram, and opposite topological properties at the valley points K and K'. In this context, two sufficient conditions guarantee the existence of TPEWs in a periodic system: the unit cell should satisfy C_3 symmetry and violate mirror symmetry [24,27,30,31]. For example, the discrete hexagonal lattice in Fig. 1(a) comprises point masses at the sublattice sites connected by linear springs of stiffness k joining nearest

neighbors. The masses move only in the out-of-plane direction, which is perpendicular to the plane of the page. Accordingly, the springs provide a force which is proportional to the relative out-of-plane displacements of neighboring masses. Each unit cell has two sites a,b where the masses are $m_a = m(1+\gamma)$ and $m_b = m(1-\gamma)$, respectively. Thus, the lattice satisfies C_3 symmetry but violates mirror symmetry about the lattice vectors C_{3v}. Two lattice types can be conveniently obtained by considering values of $\gamma > 0$ or $\gamma < 0$, which corresponds to switching the position of the masses through a mirror-symmetry operation. The band structure of the lattice with equal masses ($\gamma = 0$) shown in Fig. 1(b) reveals the presence of Dirac cones at the high-symmetry points. The symmetry is also highlighted by the isofrequency contours of the first dispersion surface, on which the path along the boundaries of the first irreducible Brillouin zone and its symmetric counterpart are represented (red solid line), along with the location of the K and K' points. The band diagrams obtained for the wave vector tracing these boundaries are shown in Fig. 1(c) in terms of the dimensionless frequency $\Omega = \omega/\omega_0$, with $\omega_0 = \sqrt{k/m}$. Comparisons are obtained for the symmetric case with equal masses ($\gamma = 0$, dashed curves) and when mirror symmetry is broken ($\gamma \neq 0$, in this case $\gamma = +0.2$, solid curves), which results in the opening of the Dirac cones to form a band gap. The bounding frequencies of the gap vary as a function of γ, and a band inversion occurs when γ changes in sign, which corresponds to the case of two mirror-symmetric unit cells [see Fig. 1(d)].

Expressing the Hamiltonian of this lattice in the basis of an extended vector combining the eigenvectors at the K and K′ valley points illustrates the analogy with the quantum valley Hall effect [2,6]. Alternatively, the topological properties of the vector bundle associated with the eigenvectors $\boldsymbol{u}_0(\boldsymbol{\kappa})$ can be used to infer the presence of interface modes [32]. The valley Chern number, which is the integral of the Berry curvature over half the Brillouin zone, characterizes the topology of this vector bundle (see [24,26]). In hexagonal lattices with broken mirror symmetry, the valley Chern number takes values $\pm 1/2$ at the opposite valleys, i.e., the K and K' points in reciprocal space, indicating opposite polarization of the corresponding eigenmodes [31] [Fig. 1(c)]. In the described discrete lattice [see Fig. 1(a)] the valley Chern number of the first mode is $(-1/2)$ $1/2$ at (K) K' points for $\gamma > 0$ and vice versa for $\gamma < 0$ [6]. To realize TPEWs, it suffices to build a structure in which two lattices with opposite valley Chern numbers share an interface. These two lattices may have the same band structure, but their eigenmodes at the valley points have opposite polarization. When these two lattices share a common interface, topologically protected localized modes exist at frequencies within the band gap [6], and TPEWs can propagate confined to that interface.

III. CONTINUOUS HEXAGONAL LATTICE

A. Configuration and material properties

The characteristics of the conceptual lattice summarized above guide the design of the continuous hexagonal elastic lattice of Fig. 2. The lattice is fabricated out of a square acrylic panel with a side of 308.4 mm and a thickness of 1.59 mm. The

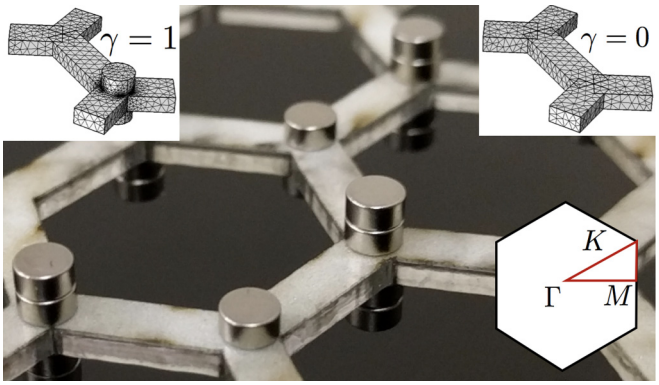

FIG. 2. Experimental lattice with added masses at the sublattice sites. Insets show the FE discretization of the unit cell for numerical study for configurations defined by $\gamma = 0$ and $\gamma = 1$, as well as the first and irreducible Brillouin zone (red solid line) for the lattice.

side of each hexagon measures $L = 10.7$ mm, while the width of the beams is $w = 3.2$ mm. The masses consist of cylindrical nickel-plated neodymium magnets ($\rho_c = 7400\,\mathrm{kg/m^3}$, $E_c = 41$ GPa, and $\nu_c = 0.28$) of height 1.5 mm and diameter 3.2 mm. The material properties of acrylic are density $\rho = 1190\,\mathrm{kg/m^3}$, Young's modulus $E = 3.2$ GPa, and Poisson's ratio $\nu = 0.35$. The lattice is generated by a set of lattice vectors $\boldsymbol{a}_1 = \sqrt{3}L\ [\sqrt{3}/2,\ -1/2]$ and $\boldsymbol{a}_2 = \sqrt{3}L\ [\sqrt{3}/2,\ 1/2]$. Unit-cell mirror symmetry is broken by adding cylindrical masses at selected sublattice sites a,b, in analogy with the discrete lattice in Fig. 1(a). The mass added by the cylinders is defined as $m_a = (|\gamma| + \gamma)m_c, m_b = (|\gamma| - \gamma)m_c$, respectively, where m_c denotes the mass of one cylinder and γ is the parameter chosen to define both the magnitude and location of the added mass at each site. Of note is the fact that the lattice is a continuous structure that is characterized by inherent mass properties defined by the density of the material. Therefore, the terms m_a,m_b denote the added mass at the sublattice sites. An even number of cylinders is added at each location in order to preserve symmetry in the thickness direction and for practical purposes in the experimental implementation of the concept, whereby attracting magnetic cylinders are clamped at the desired location. Hence, values $\gamma > 0$ describe the addition of masses at site a, while $\gamma < 0$ corresponds to an added mass in b. In addition, the case $\gamma = +1$ (-1) describes the addition of two cylinders in a (b), and finally, the case when $\gamma = 0$ corresponds to the case of no additional masses.

B. Dispersion analysis

1. Unit cell

The dispersion properties of the lattice are estimated based on the finite-element (FE) discretization of the lattice modeled as a three-dimensional continuous solid. In the model, the motion of each material point within the domain at the generic location x,y,z is governed by the standard equations of linear elasticity for an isotropic medium [33],

$$\rho\ddot{\boldsymbol{u}} - [(\lambda + \mu)\nabla(\nabla \cdot \boldsymbol{u}) + \mu\nabla^2\boldsymbol{u}] = 0, \qquad (1)$$

where $\boldsymbol{u}(x,y,z) = u_x\boldsymbol{i} + u_z\boldsymbol{j} + u_z\boldsymbol{k}$ is the displacement vector and $\boldsymbol{i}$, $\boldsymbol{j}$, $\boldsymbol{k}$ denote the unit vectors along the x,y,z directions.

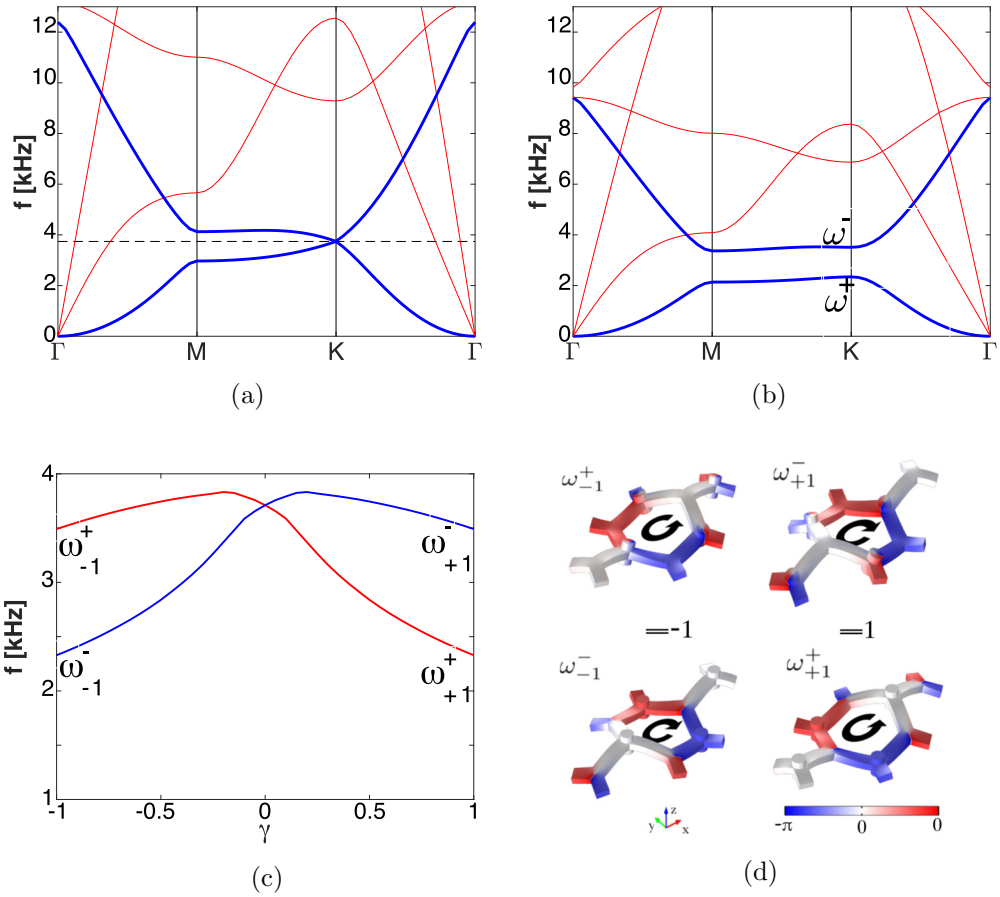

FIG. 3. Dispersion diagrams: (a) lattice without masses, $\gamma = 0$; (b) lattice with masses, $\gamma = 1$ (thin dashed black line: location of the Dirac point, thick blue lines: out-of-plane wave mode, thin red lines: shear polarized modes). (c) Variation of band gap bounding frequencies ω^+ (red line) and ω^- (blue line) at K as a function of γ showing band inversion and (d) phase of corresponding eigenfunctions of the first two out-of-plane modes at K for $\gamma = -1$ and $\gamma = 1$.

Also, λ and μ are the Lamé constants of the solid. For reference, here and in the remainder of the paper, the x, y directions define the plane of the lattice, while the z direction is the thickness, or out-of-plane, direction. The solid is patterned according to the hexagonal topology considered herein and is discretized for analysis within the COMSOL MULTIPHYSICS environment. Each unit cell is discretized using around 20 000 second-order tetrahedral elements which produce the mesh shown in the insets of Fig. 2. Upon discretization, imposing a plane-wave solution along with the enforcement of Floquet-Bloch conditions to the unit-cell degrees of freedom leads to a linear eigenvalue problem that is solved in terms of frequency for a wave vector varying along the edge of the first irreducible Brillouin zone for the lattice under consideration. Results for lattices characterized by $\gamma = 0$ and $\gamma = 1$ are shown in Figs. 3(a) and 3(b).

The dispersion analysis predicts multiple wave modes that correspond to the numerous degrees of freedom in the considered FE unit-cell model. Each node has three degrees of freedom, which is reflected by the three branches emanating from the Γ point at zero frequency. In the long-wavelength limit, the lattice approaches the behavior of a thin plate and is characterized by a flexural, or out-of-plane, mode and two in-plane modes which can be described as "shear" and "longitudinal-like." Consistent with its flexural nature, the out-of-plane mode is characterized by a parabolic dispersion branch at long wavelengths, and it is loosely coupled with the in-plane modes. This makes its identification based on the eigenvector components relatively simple (see thick blue line in Fig. 3). In contrast, the modes that are mostly in-plane polarized, i.e., that are associated with eigenvectors where $u_x, u_y \gg u_z$ (red lines in Fig. 3), are significantly more difficult to differentiate from one another. However, their distinct representation goes beyond the scope of the work, which focuses on the out-of-plane mode.

In analogy with the discrete lattice, the hexagonal lattice with no masses attached ($\gamma = 0$) has C_{3v} symmetry. In addition, a Dirac point at the frequency identified by the horizontal dashed line is observed for the out-of-plane branches at the K point of the reciprocal lattice space [Fig. 3(a)]. Adding two cylindrical masses at the a site ($\gamma = 1$) breaks mirror symmetry and produces a band gap [see Fig. 3(b)]. The bounding frequencies of the gap, denoted ω^+ and ω^-, are tracked as a function of γ, which produces the plot of Fig. 3(c), where a band inversion is observed. The eigenfunctions $\boldsymbol{U}$ associated with these eigenvalues for $\gamma = -1$ and $\gamma = 1$ are depicted in Fig. 3(d), which also illustrate the predominantly out-of-plane polarization of these modes (see Supplemental Material [34] for animations of the first two out-of-plane modes at K for $\gamma = 1$). We observe that, while the eigenvalues

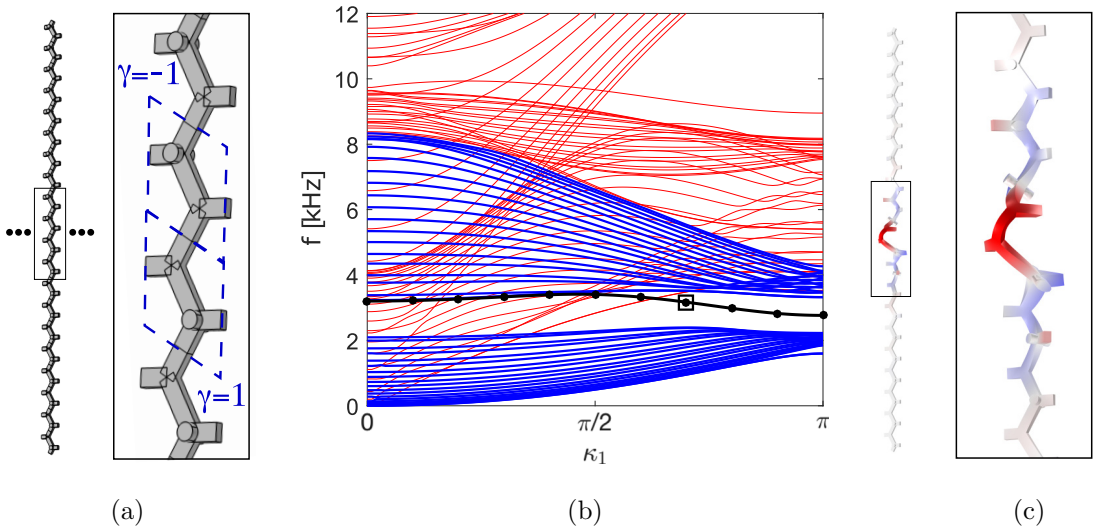

FIG. 4. (a) Finite strip and close-up of the topological interface. (b) Dispersion diagram: edge mode (black line with dots), out-of-plane modes (thick blue lines), and in-plane polarized modes (thin red lines). (c) Eigenvector corresponding to the edge mode evaluated for wave number $\kappa_x = 0.7\pi$ at $f \simeq 3$ kHz.

are preserved under the transformation $\gamma \to -\gamma$ due to time-reversal symmetry, the eigenfunctions feature different polarizations that reflect the mirror-symmetry relations of the corresponding unit cells. The transformation $\gamma \to -\gamma$ may be achieved by simply reversing the direction of the lattice basis vectors, so the positions of the sublattice sites a and b are switched. Due to the broken C_{3v} mirror symmetry, a reflection changes the eigenfunctions and thereby the band topology [2]. Let us examine in detail the phase of the eigenfunctions $\boldsymbol{U}$ at the K point. Note that for $\gamma < 0$ the eigenfunction of the first mode has clockwise polarization, and the eigenfunction of the second one has counterclockwise polarization, whereas the opposite is observed for $\gamma > 0$. Figure 3(c) shows that the bands are inverted when γ changes sign (at $\gamma = 0$). Furthermore, the K' points have polarizations opposite those of the K points due to time-reversal symmetry. The change in polarization across $\gamma = 0$ suggests that lattices with $\gamma > 0$ and $\gamma < 0$ have opposite valley Chern numbers [6,35] and that TPEWs are expected to exist along an interface between a lattice with $\gamma > 0$ and a lattice with $\gamma < 0$ at frequencies within the common band gap.

2. *Finite strip*

The dispersion analysis of a strip including a finite number of cells and an interface is conducted to evaluate the existence of edge and interface modes. The study is based on the FE model previously considered for the unit cell, extended to include the finite strip assembly in Fig. 4(a). The strip consists of ten unit cells of the type $\gamma = 1$ and ten unit cells with $\gamma = -1$, which, as discussed in the previous section, are characterized by different topologies. The top and bottom boundaries of the strip are considered free, which is a choice that does not affect the existence of the interface mode. The corresponding dispersion diagram is presented in Fig. 4(b), where, again, the out-of-plane modes are easily distinguished from the in-plane polarized ones through the evaluation of the displacement components of the eigenvectors and are denoted by the thick blue lines. In addition to these bulk modes, two modes appear in the band gap, one of which is a mode localized at the interface (black dotted line), while the second mode is localized at the boundaries of the strip (black line). One eigenvector corresponding to the interface mode is displayed in Fig. 4(c), which shows the displacement field of the edge mode for $\kappa_x = 0.7\pi$ and frequency $f = 3$ kHz. The dispersion study shows that in spite of the large number of modes present and of the fact that the band gap is associated with only the out-of-plane modes and is therefore only partial, the topological differences between the two lattices still lead to topologically protected interface modes.

IV. EXPERIMENTAL RESULTS

A. Experimental setup

The numerical simulations described in the previous section guide the design and experimental characterization of the considered hexagonal lattice. The lattice is cut out of an acrylic panel according to the dimensions described in Sec. III. In the experiments, the lattice is held in a vertical position by a vice that clamps its lower left corner. In addition, commercially adhesive putty tape is added along the boundaries for absorption of incoming waves and to minimize reflections which may affect the visualization of the propagation of the interface modes. Wave motion in the lattice is induced by lead zirconate titanate (PZT) disks bonded at selected locations and driven by a voltage signal generated by a signal generator upon amplification. The PZT disks are bonded to the top surface of the lattice. When the voltage is applied, they induce a distribution of shear stresses at the bonded interface, which generates both the in-plane and out-of-plane motion of the lattice. Full-field response of the lattice is recorded through a scanning laser Doppler vibrometer (SLDV), which measures the out-of-plane velocity of points belonging to a predefined measurement grid. Given the SLDV limitation to measurements of only the out-of-plane motion, no contribution

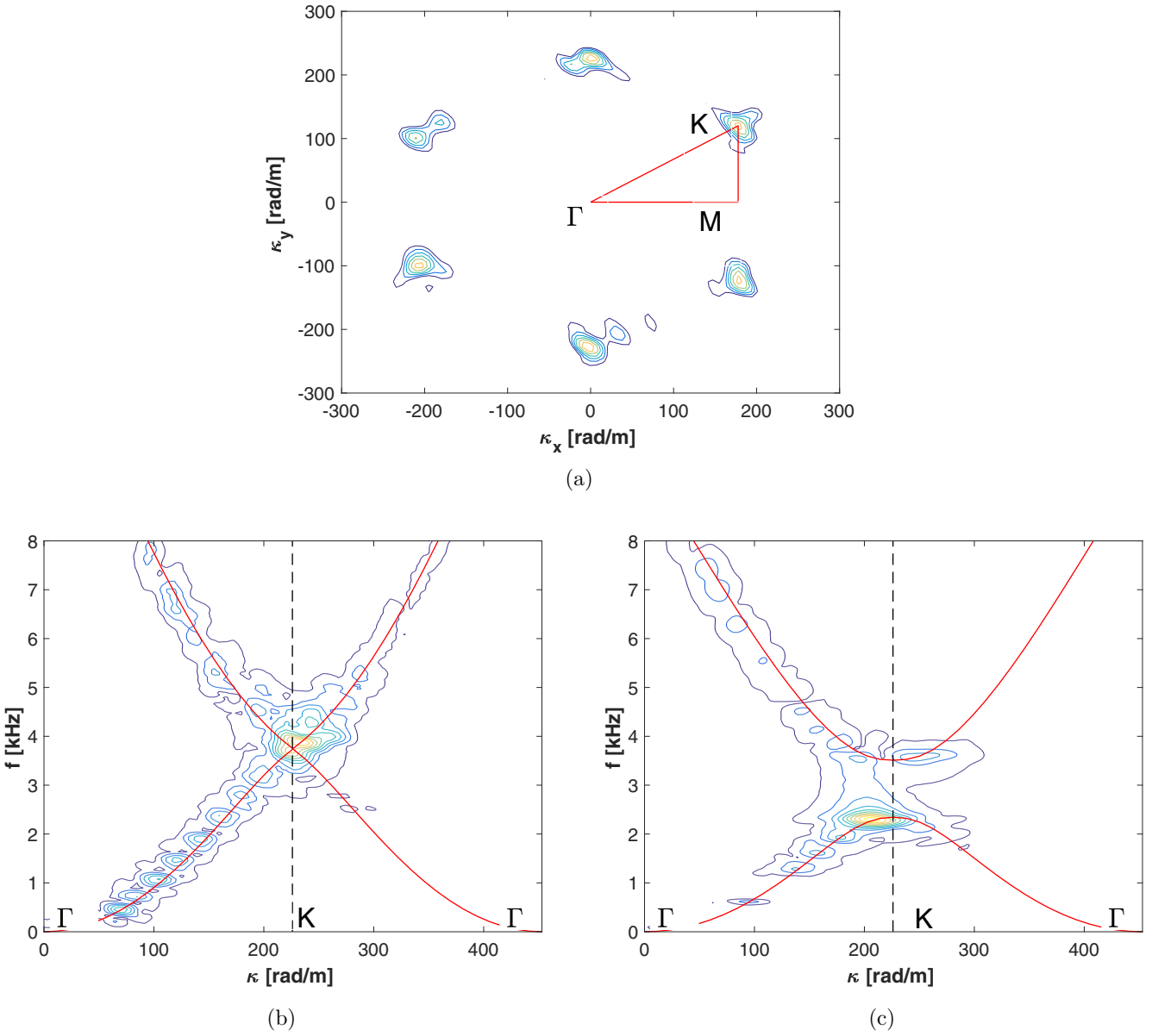

(a)

(b)

(c)

FIG. 5. Experimental 3D-FTs. (a) Lattice with $\gamma = 0$: cross section $|\hat{w}(\kappa_x,\kappa_y,\omega_0)|$ at frequency $f_0 \approx 3.75$ kHz close to the numerically predicted Dirac cone. Frequency/wave-number representation $|\hat{w}(\kappa|_{\mathcal{C}},\omega)|$ along the path $\mathcal{C}$: Γ-K-Γ and comparison with COMSOL predictions (solid red line): lattice with (b) $\gamma = 0$ and (c) $\gamma = 1$.

from in-plane modes is observed in the measured responses. While the equipment records one point at a time, repeating the excitation to record the response at every measurement location and the tracking of the phase between subsequent measurements allows the recording of the full-field wave motion of the lattice. The measurements include seven points along the side L of the hexagon, so that a total of 3670 points are recorded over the entire lattice. After recording, the wave-field data are interpolated on a regular rectangular grid that includes 100 points along the horizontal (x) and vertical (y) extent of the measurement domain. The excitation consists of broadband frequency pulses that cover the frequency range of interest, which is up to 12 kHz. This is achieved through modulated sinusoidal pulses and their superposition or half-cycle pulses whose duration defines the frequency bandwidth of the excitation.

B. Estimation of the dispersion properties

The measurements and their subsequent interpolation produce a data set in the form of a matrix $w(x,y,t)$ that describes the evolution of the deflection of the lattice in time. The matrix of the experimental results is analyzed in Fourier space by performing a three-dimensional Fourier transformation (3D-FT), which gives [36]

$$\hat{w}(\kappa_x,\kappa_y,\omega) = \mathcal{F}_{3D}[w(x,y,t)].$$

The resulting quantity describes the spectral content, in terms of both frequency and reciprocal space, of the recorded wave field. Cross sections along defined wave paths $\mathcal{C}$, i.e., $\hat{w}(\kappa|_{\mathcal{C}},\omega)$, illustrate the spectral content as a function of frequency for the wave vector varying along specific lattice directions, while evaluation at one frequency ω_0,

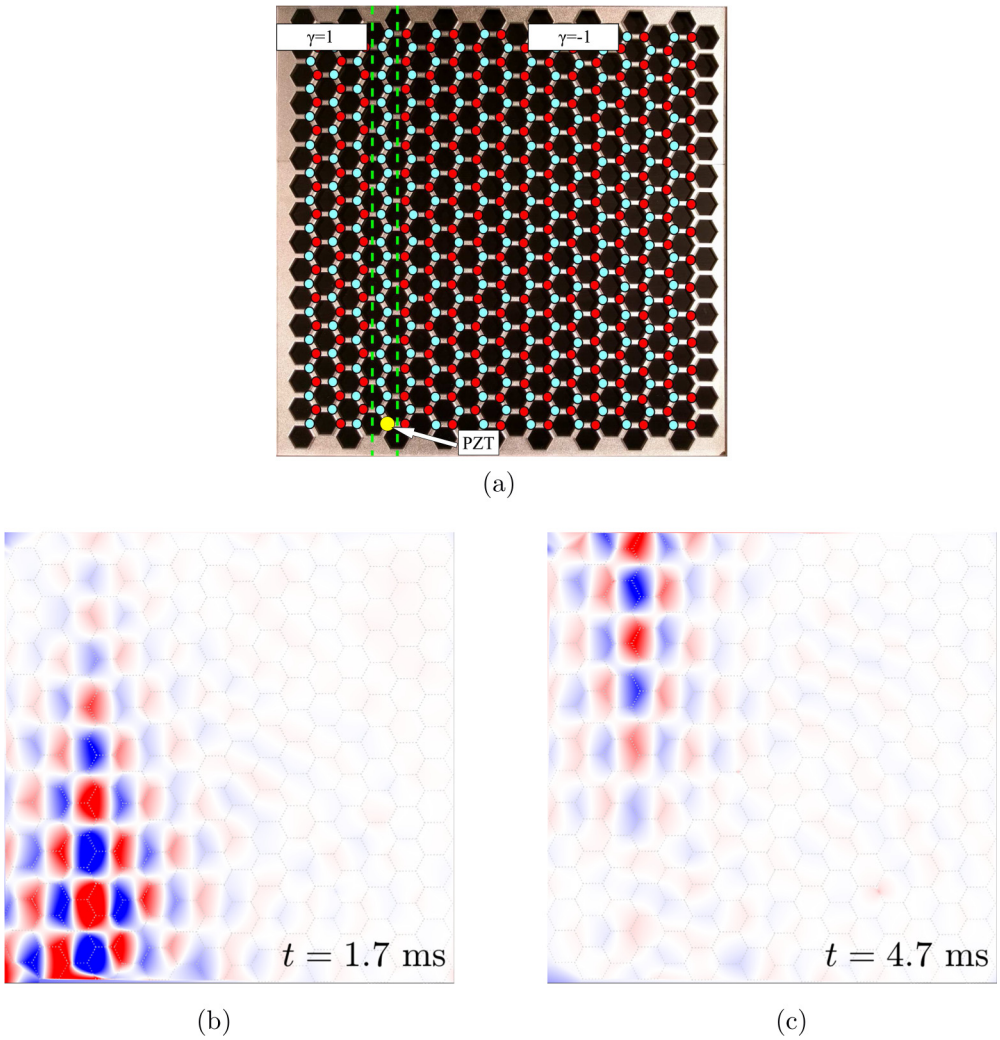

FIG. 6. (a) Line interface (red dots indicate two masses attached at the sublattice sites, and cyan dots denote locations where no masses are added) with $\gamma = 1$ (-1) on the left (right). (b) and (c) Snapshots of measured wave motion at two instants of time. Excitation is an 11-cycle tone burst at 3 kHz (contours are normalized by the displacement amplitude of 3×10^{-8} m).

i.e., $\hat{w}(\kappa_x,\kappa_y,\omega_0)$, illustrates the distribution of energy in the reciprocal wave-number space at that frequency. These maps provide direct visualization of the dispersion characteristics of the domain of interest and are therefore used to validate the numerical predictions for the lattice under consideration.

We first verify experimentally the dispersion diagrams of the acrylic hexagonal lattice with the $\gamma = 0$ configuration (no masses attached). The elastic lattice is excited at its center using a PZT disk that applies a pulse of 40 μs to excite frequencies up to 12.5 kHz. Figure 5(a) displays the magnitude $|\hat{w}(\kappa_x,\kappa_y,\omega_0)|$ of the 3D-FT at a frequency of $f_0 = \omega_0/(2\pi) \approx 3.75$ kHz, which is close to the Dirac cone frequency identified by the numerical study of dispersion [see Fig. 3(a)]. The contours correspond to the magnitude $|\hat{w}|$, which is not of particular interest here. Most relevant is their location: they are localized at the high-symmetry points and effectively illustrate a condition that defines a Dirac point. For reference, the boundaries of the first irreducible Brillouin zone are shown along with the points defining its boundary. The size of the zone is defined by a lattice vector $a = \sqrt{3}L \approx 18.4$ mm, which corresponds to the magnitude of the wave vector at the K point of $\kappa \approx 226$ rad/m. Next, results are presented in terms of frequency/wave-number content by considering a cross section of the 3D-FT along the path $\mathcal{C}$: Γ-K-Γ for $\gamma = 0$ (no masses added). Figure 5(b) illustrates the dispersion branches detected during the experiments, which compare very well with the COMSOL predictions (solid red line). The case of $\gamma = 1$ is then tested, and Fig. 5(c) displays the results in the frequency/wave-number domain. An opening of the band gap at the K point is observed as predicted by the COMSOL simulations, again represented by the solid red line superimposed on the contours.

C. Experimental observation of topologically protected interface waves

The dispersion studies and the experimental setup developed allow the investigation of the existence of topologically protected modes at the interface of lattices consisting of unit cells that are inverted copies of each other ($\gamma = -1$ and $\gamma = 1$). This is easily achieved by placing magnetic cylinders

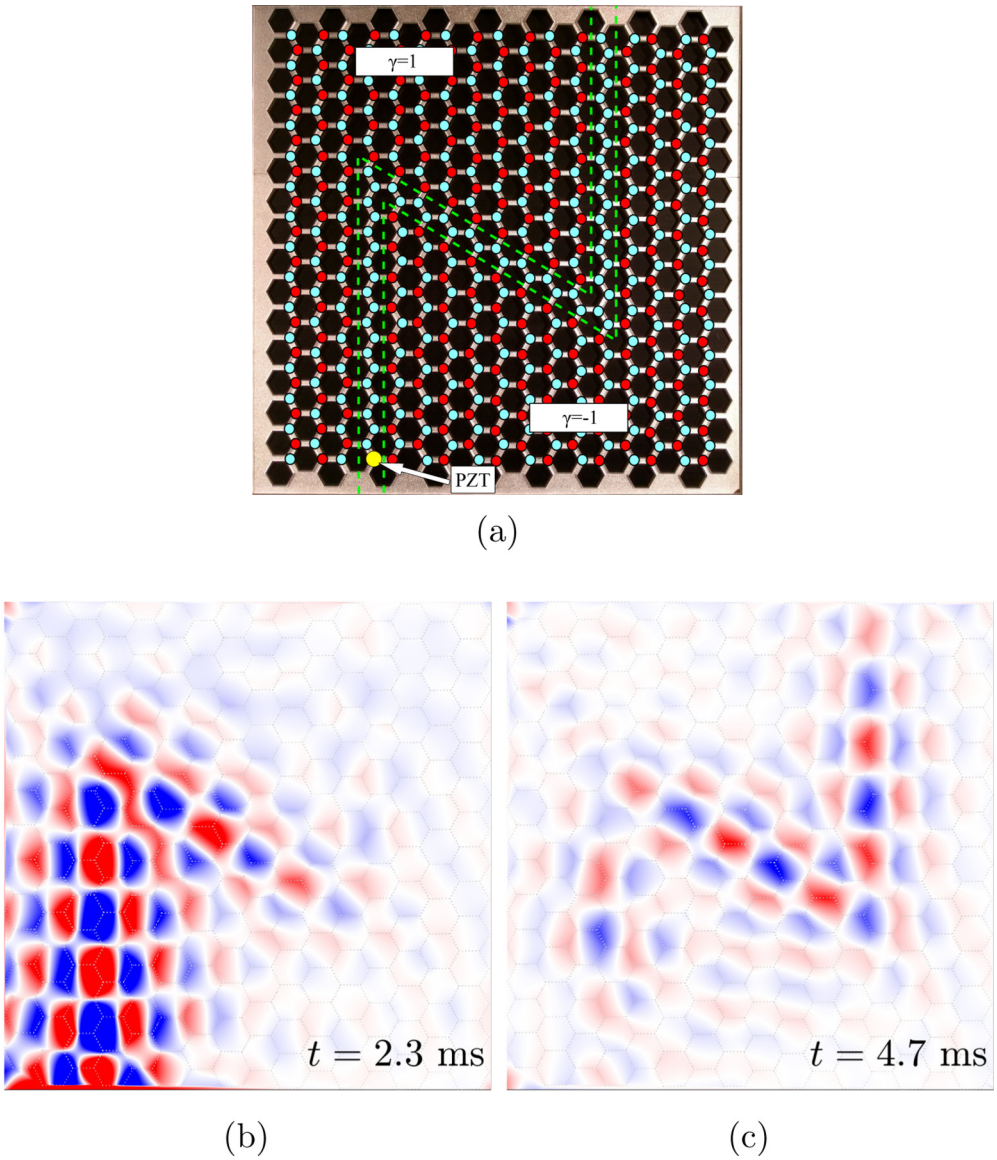

FIG. 7. (a) A nontrivial N-shaped interface (red dots indicate two masses attached at the sublattice sites, and cyan dots denote locations where no masses are added) with $\gamma = 1$ (-1) on the left (right). (b) and (c) Snapshots of measured wave motion at two instants of time. Excitation is an 11-cycle tone burst at 3 kHz (contours are normalized by the displacement amplitude of 1.5×10^{-8} m).

as added masses at the selected locations, so that a variety of interfaces can be introduced and tested.

We first investigate the straight-line interface shown in Fig. 6(a). The cylindrical masses are placed so that the unit cells to the left of the interface have $\gamma = 1$ and those to the right have $\gamma = -1$. Note that this interface has zero width, and the green lines in the figure indicate only the path that TPEWs are expected to follow. The structure is excited at the location shown with a tone-burst signal of 11 cycles at a frequency of 3 kHz. The considered signal has a bandwidth of approximately 1 kHz and therefore excites a relatively broad frequency range which falls entirely within the band gap. Figures 6(b) and 6(c) display time snapshots of the measured out-of-plane displacement by plotting the contours of the interpolated wave field (see Supplemental Material [34] for an animation of the measured out-of-plane displacement). As indicated above, the displacement field shown is an interpolation over a rectangular grid of the measured response in points belonging to the lattice. This produces a continuous representation which facilitates visualization of the results along with the overlay of the geometry of the lattice represented as thin black lines. The contours are normalized by the maximum displacement amplitude of 3×10^{-8} m. Figures 6(b) and 6(c) illustrate how the induced out-of-plane wave travels along the interface and has limited penetration into the bulk. The results also show that the amplitude decays below 10% of the original value in approximately four unit cells, which is a number consistent with observations from similar investigations presented in the literature [28]. The number of unit cells in our lattice (18×16) and their size was set according to convenience of fabrication and testing and are quite limited. Future designs may be scaled in order to include a larger number of units that may lead to a reduction in the lateral spreading of the interface modes. The rate of spatial decay may affect the results in Fig. 6(a)

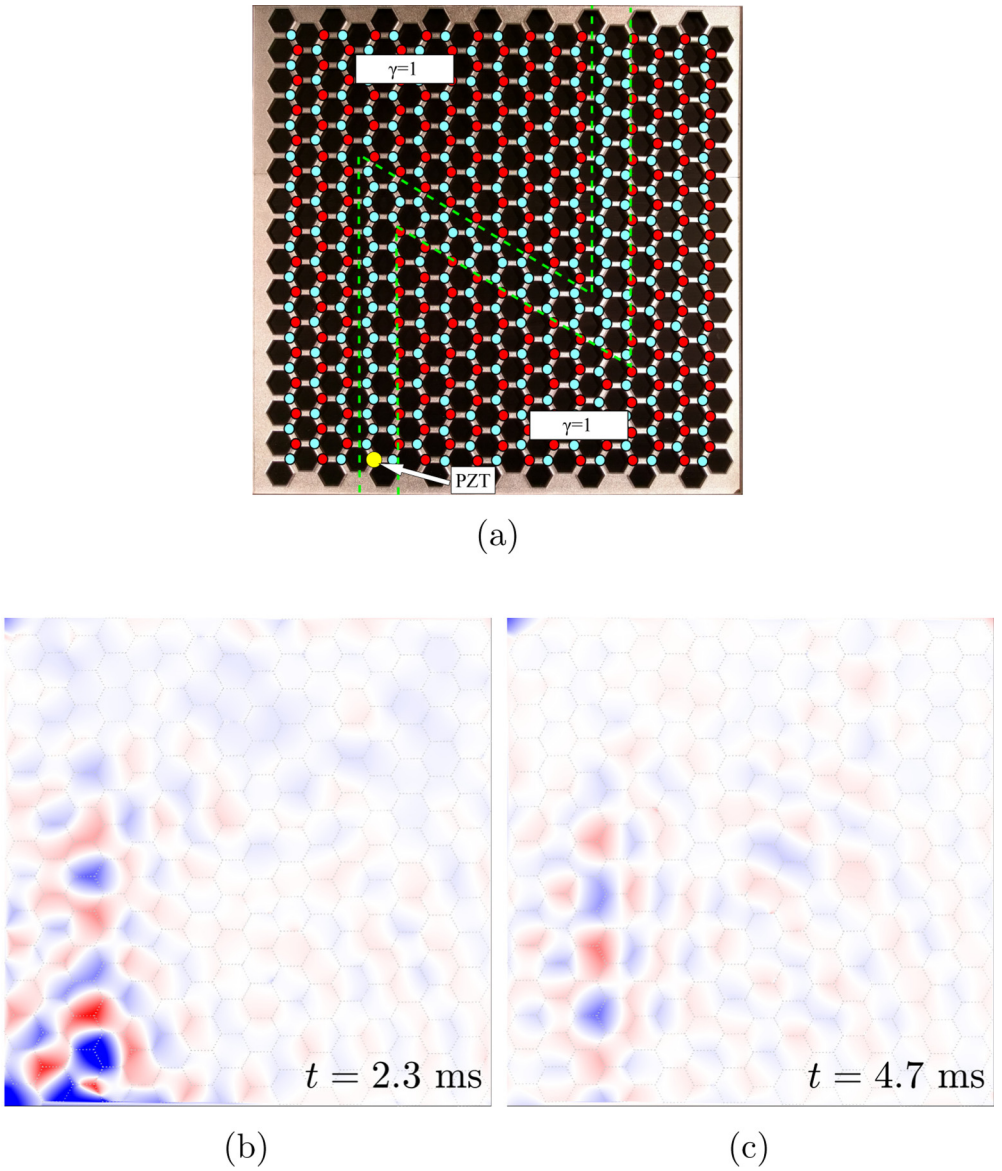

FIG. 8. (a) N-shaped trivial interface (red dots indicate two masses attached at the sublattice sites, and cyan dots denote locations where no masses are added) with $\gamma = 1$ everywhere. (b) and (c) Snapshots of measured wave motion at two instants of time. Excitation is an 11-cycle tone burst at 3 kHz (contours are normalized by the displacement amplitude of 1.5×10^{-8} m).

due to the proximity of the source from the boundary. Videos showing the time evolution of the displacement field based on measurements are provided in the Supplemental Material [34].

The excited in-plane waves, not measured in the experiment, do not exhibit a band gap at the targeted frequencies and therefore are allowed to travel on both sides of the interface. Of interest is the fact that the interface mode (for out-of-plane waves) is still observable after it reaches the boundary opposite the excitation location, although the amplitude is reduced by material dissipation that is particularly noticeable in the acrylic substrate utilized for the tests. The choice of acrylic as the material for the experiments is driven by considerations of convenience of fabrication and cost. In further studies, the use of metallic lattices, such as aluminum, will be considered for investigations of effects such as the extent of propagation and attenuation along the interface and interactions with boundaries and defects. These interactions are not studied as part of this work but are important aspects of follow-on investigations for the characterization of the robustness of this class of modes.

A second example considers an N-shaped zero-width interface with segments parallel to the lattice vectors [Fig. 7(a)]. The objective is to observe the behavior of the wave in the presence of 120° corners along the interface. The cylindrical masses are attached so that the unit cells to the top left of the interface have $\gamma = 1$ and those to the bottom right have $\gamma = -1$. The results in Figs. 7(b) and 7(c) show the propagation of the wave along the N-shaped topological interface and a limited propagation into the bulk. Furthermore, the wave manages the 120° turn, illustrating the ability to change direction with limited backscattering. The contours are normalized by the displacement amplitude 1.5×10^{-8} m. (See the Supplemental Material [34] for an animation showing the measured out-of-plane displacement).

We compare the results above to the case of a waveguide obtained by removing a unit cell from an otherwise periodic domain, which leads to a trivial (nontopological) interface. To this end, masses are attached so that all unit cells have $\gamma = 1$. The N-shaped interface within one lattice type is thus obtained by simply removing a line of masses, as illustrated in Fig. 8(a), which corresponds to a nonzero-width interface. The resulting lattice response in Figs. 8(b) and 8(c) illustrates the limited ability of the wave to enter and propagate along the interface. (See the Supplemental Material [34] for an animation of the measured out-of-plane displacement). The induced motion of the lattice appears to remain localized in the vicinity of the excitation point and eventually decays as a result of material dissipation. Comparing the amplitude of transmitted waves, we conclude that the amount of energy traveling through the interface is much lower in this case, in spite of the nonzero width of the interface. This test is here based on the fact that for this nonzero-width interface, the dispersion properties are those of a lattice without added masses for which the flexural band gap does not exist. Thus, the goal here is to illustrate that removal of a single row from a periodic assembly is not sufficient to guarantee propagation.

V. CONCLUSIONS

Control of mechanical waves is applicable in many technological fields of interest, including detection, energy harvesting, and telecommunications. This study demonstrated the existence of interface modes within the band gap of a two-dimensional elastic hexagonal lattice and the propagation of TPEWs exploiting a mechanical analog of the quantum valley Hall effect. This phenomenon allows creating a simple and robust waveguide for elastic waves in a wide range of frequencies. Guided by studies on conceptual lattices and numerical simulations, experiments were conducted to predict the dispersion properties of the considered hexagonal lattices and to explore the existence of TPEWs along predefined interfaces. The difference in propagation along nontrivial interfaces is also illustrated through an experiment that reveals the difference of modes of propagation endowed with topological protection from those that are obtained by introducing a line defect in an otherwise periodic assembly. The experimental configurations illustrated herein are suitable for potential implementation of the concept to phononic systems and structural components and could be further utilized to investigate the sensitivity of these configurations to a variety of defect and interface configurations.

ACKNOWLEDGMENTS

The authors acknowledge the support of the US Air Force Office of Scientific Research (Grants No. FA9550-13-1-0122 and No. FA9550-15-1-0397) and of the National Science Foundation (Grant No. 1332862).

[1] S. Huber, Nat. Phys. **12**, 621 (2016).
[2] C. Brendel, V. Peano, O. Painter, and F. Marquardt, arXiv:1701.06330.
[3] A. B. Khanikaev, S. H. Mousavi, W.-K. Tse, M. Kargarian, A. H. MacDonald, and G. Shvets, Nat. Mater. **12**, 233 (2013).
[4] L. Lu, J. D. Joannopoulos, and M. Soljačić, Nat. Photonics **8**, 821 (2014).
[5] S. H. Mousavi, A. B. Khanikaev, and Z. Wang, Nat. Commun. **6**, 8682 (2015).
[6] R. K. Pal and M. Ruzzene, New J. Phys. **19**, 025001 (2017).
[7] V. Peano, C. Brendel, M. Schmidt, and F. Marquardt, Phys. Rev. X **5**, 031011 (2015).
[8] N. Swinteck, S. Matsuo, K. Runge, J. Vasseur, P. Lucas, and P. Deymier, J. Appl. Phys. **118**, 063103 (2015).
[9] H. Nassar, X. Xu, A. Norris, and G. Huang, J. Mech. Phys. Solids **101**, 10 (2017).
[10] E. Prodan and C. Prodan, Phys. Rev. Lett. **103**, 248101 (2009).
[11] L. Nash, D. Kleckner, A. Read, V. Vitelli, A. Turner, and W. Irvine, Proc. Natl. Acad. Sci. USA **112**, 14495 (2015).
[12] A. B. Khanikaev, R. Fleury, S. H. Mousavi, and A. Alù, Nat. Commun. **6**, 8260 (2015).
[13] R. Pal, M. Schaeffer, and M. Ruzzene, J. Appl. Phys. **119**, 084305 (2016).
[14] C. He, Z. Li, X. Ni, X. Sun, S. Yu, M. Lu, X. Liu, and Y. Chen, Appl. Phys. Lett. **108**, 031904 (2016).
[15] R. Süsstrunk and S. Huber, Science **349**, 47 (2015).
[16] J. Ningyuan, C. Owens, A. Sommer, D. Schuster, and J. Simon, Phys. Rev. X **5**, 021031 (2015).
[17] E. Prodan, K. Dobiszewski, A. Kanwal, J. Palmieri, and C. Prodan, Nat. Commun. **8**, 14587 (2017).
[18] R. Chaunsali, E. Kim, A. Thakkar, P. G. Kevrekidis, and J. Yang, Phys. Rev. Lett. **119**, 024301 (2017).
[19] M. Xiao, G. Ma, Z. Yang, P. Sheng, Z. Zhang, and C. Chan, Nat. Phys. **11**, 240 (2015).
[20] C. Kane and T. Lubensky, Nat. Phys. **10**, 39 (2014).
[21] J. Paulose, A. Meeussen, and V. Vitelli, Proc. Natl. Acad. Sci. USA **112**, 7639 (2015).
[22] D. Z. Rocklin, B. G.-g. Chen, M. Falk, V. Vitelli, and T. C. Lubensky, Phys. Rev. Lett. **116**, 135503 (2016).
[23] D. Z. Rocklin, New J. Phys. **19**, 065004 (2017).
[24] D. Xiao, W. Yao, and Q. Niu, Phys. Rev. Lett. **99**, 236809 (2007).
[25] F. Zhang, J. Jung, G. A. Fiete, Q. Niu, and A. H. MacDonald, Phys. Rev. Lett. **106**, 156801 (2011).
[26] F. Zhang, A. H. MacDonald, and E. J. Mele, Proc. Natl. Acad. Sci. USA **110**, 10546 (2013).
[27] T. Ma and G. Shvets, New J. Phys. **18**, 025012 (2016).
[28] J. Lu, C. Qiu, L. Ye, X. Fan, M. Ke, F. Zhang, and Z. Liu, Nat. Phys. **13**, 369 (2017).
[29] L. Ye, C. Qiu, J. Lu, X. Wen, Y. Shen, M. Ke, F. Zhang, and Z. Liu, Phys. Rev. B **95**, 174106 (2017).
[30] J. Lu, C. Qiu, M. Ke, and Z. Liu, Phys. Rev. Lett. **116**, 093901 (2016).
[31] X.-D. Chen, F.-L. Zhao, M. Chen, and J.-W. Dong, Phys. Rev. B **96**, 020202(R) (2017).

[32] D. Carpentier, in *Dirac Matter*, edited by B. Duplantier, V. Rivasseau, and J. N. Fuchs, Progress in Mathematical Physics, Vol. 71 (Birkhäuser, Cham, Basel, Switzerland, 2017), pp. 95–129.

[33] J. Achenbach, *Wave Propagation in Elastic Solids*, North-Holland Series in Applied Mathematics and Mechanics, Vol. 16 (Elsevier, Amsterdam, 2012).

[34] See Supplemental Material at http://link.aps.org/supplemental/10.1103/PhysRevB.96.134307 for animations of FE simulations and animations of measured displacements in experiments.

[35] T. Fösel, V. Peano, and F. Marquardt, New J. Phys. (2017), doi: 10.1088/1367-2630/aa8a9f.

[36] T. E. Michaels, J. E. Michaels, and M. Ruzzene, Ultrasonics **51**, 452 (2011).